



Correlation between plasma electrolytic oxidation treatment stages and coating microstructure on aluminum under unipolar pulsed DC mode



Vahid Dehnavi ^{a,*}, Ben Li Luan ^{b,c,e,1}, Xing Yang Liu ^{d,2}, David W. Shoesmith ^{e,3}, Sohrab Rohani ^{f,4}

^a Department of Chemical and Biochemical Engineering, The University of Western Ontario, London, ON N6A 5B9, Canada

^b National Research Council Canada, 800 Collip Circle, London, ON N6G4X8, Canada

^c Department of Chemistry, The University of Western Ontario, London, ON N6A 5B7, Canada

^d National Research Council Canada, 800 Collip Circle, London ON, N6G4X8, Canada

^e Surface Science Western, Department of Chemistry, The University of Western Ontario, London, ON N6A 5B7, Canada

^f Department of Chemical and Biochemical Engineering, The University of Western Ontario, London, ON N6A 5B9, Canada

ARTICLE INFO

Available online 8 November 2014

Keywords:

Plasma electrolytic oxidation

Electrical parameters

Voltage–time response

Morphology

Microhardness

Coating

ABSTRACT

Alumina coatings were deposited on 6061 aluminum alloy substrates using plasma electrolytic oxidation (PEO) in an alkaline silicate electrolyte. Different electrical parameters, including frequency, duty cycle, and current density were applied to obtain PEO coatings. Scanning electron microscopy (SEM) and microhardness tests were used to investigate the coating microstructure and properties. For each sample, the voltage–time response of the PEO process was obtained and compared with surface morphology, and coating cross sections and thicknesses. Special consideration was given to the connection between the electrical parameters, different stages of the PEO process, and the morphology and microstructure of the coatings. Applying different electrical parameters changed the duration and ratio of the PEO stages in the voltage–time response curve and affected the growth rate, surface morphology, microstructure and microhardness of the coatings. We report the new finding of a correlation between the stage of the PEO process and the microstructure and morphology of the coating.

Crown Copyright © 2014 Published by Elsevier B.V. All rights reserved.

1. Introduction

Plasma electrolytic oxidation (PEO) is a surface modification technique capable of producing oxide coatings with desirable properties on the surface of valve metals and alloys. PEO is an electrochemical process in which coatings are formed as a result of the oxidation of the substrate material via a series of localized electrical discharge events in an aqueous electrolyte [1–3].

Coatings prepared by PEO have been successfully produced on aluminum, magnesium and titanium substrates. Recently researchers have applied this technique to zirconium [4–6] and tantalum [7,8] as well. PEO coatings have existing and potential applications in a wide range of industry sectors. Examples of these applications include wear [9–12] and corrosion [13–15] resistant coatings, thermal barrier coatings [3,16,17], coatings for infrared concealment [18] and biocompatible coatings for implants [19–21].

Different techniques and methods have been employed by various researchers to study the PEO coating growth behavior and the phenomena occurring during the process. To study the micro-discharge behavior during PEO treatment of various substrate materials, researchers have used real-time imaging techniques. The results of the studies on different substrates such as aluminum [22, 23], magnesium [24], titanium [25,26] and zirconium [5,27] revealed the spatial density, intensity, distribution and lifetime of the micro-discharges. Optical emission spectroscopy (OES) has been utilized to identify the elements present in the plasma and also to estimate the plasma temperature during PEO in aluminum [28–30], magnesium [31] and titanium [32].

Generally up to four stages are reported during PEO [28,33]. PEO typically starts with an abrupt linear increase in the voltage, which corresponds to the conventional anodic oxidation, followed by the appearance of micro-discharges on the surface of the sample as a result of dielectric breakdown after the breakdown voltage is reached. As the plasma coating process proceeds, the characteristics of the micro-discharges including their intensity, spatial density and color vary during subsequent stages of the process. The individual and collective characteristics of the micro-discharges, generated during the PEO process, determine the thermal and chemical conditions of the coating process and as a result play a key role in the formation of the oxide coatings and affect the structure, morphology, phase formation and distribution in the coatings [5].

* Corresponding author. Tel.: +1 519 702 5582.

E-mail addresses: vdehnavi@uwo.ca, vdehnavi@gmail.com (V. Dehnavi), Ben.Luan@nrc-cnrc.gc.ca (B.L. Luan), XingYang.Liu@nrc-cnrc.gc.ca (X.Y. Liu), dwshoesm@uwo.ca (D.W. Shoesmith), srohani@uwo.ca (S. Rohani).

¹ Tel.: +1 519 430 7043.

² Tel.: +1 519 430 7042.

³ Tel.: +1 519 661 2111x86366.

⁴ Tel.: +1 519 661 4116.

The phenomenon and mechanism happening in each stage during PEO and the resulting effects on the oxide layer growth behavior are different. Applied process parameters can change the duration and ratio of these stages which in turn could result in coatings with different morphology, microstructure and phase composition [34].

Different applications require PEO coatings with unique properties. A dense coating, free from pores and defects could be a good candidate for corrosion protection, and the porosity in the PEO layer could be used as a base for sealants and primers to improve corrosion protection [35]. Microporosity in the coatings on the surface of implants is beneficial and could have several functions including helping bone tissue in-growth and acting as a depot for bioactive constituents [36]. Controlling the PEO process to yield the desired morphology and microstructure for specific applications is a key requirement for the success of this method in industry.

The voltage–time response of the PEO process can provide readily measurable and useful information about the different stages occurring during PEO. Investigating the correlation between coating characteristics and different stages of PEO can improve understanding of, and provide more control over, the process. Despite the useful information that could be derived from the voltage–time response, studies addressing the correlation between voltage–time curves and coating properties are very scarce. This research investigates the effect of electrical parameters, including applied current density, frequency and duty cycle, on the voltage–time behavior during PEO and its correlation with the morphology and microstructure of the coatings.

2. Materials and methods

A unipolar, pulsed DC PEO coating unit was used to coat 6061 aluminum alloy (nominal chemical composition (wt%): 0.40–0.80% Si, 0.70% Fe, 0.15–0.40% Cu, 0.15% Mn, 0.80–1.20% Mg, 0.04–0.35% Cr, 0.25% Zn, 0.15% Ti, and balance Al) disk coupons with an average diameter of ~30 mm and a thickness of ~8 mm. The coupons were manually ground up to 600 grit using silicon carbide abrasive papers. After cleaning with isopropanol, they were rinsed and dried using compressed air. The coatings were prepared in an aqueous alkaline electrolyte containing 2 g/l Na_2SiO_3 and 2 g/l KOH in deionized water. The temperature of the electrolyte was kept below 40 °C by an external heat exchanger/chiller. Samples were treated at two frequencies, 50 and 1000 Hz, at duty cycles (D_t) of 20% and 80% with current densities (J) of 5, 10, 15, 20, and 25 A/dm². The duty cycle (D_t) is the percentage of the on-time, t_{on} , during a single pulse. A schematic of the pulse wave form and the corresponding electrical parameters of the unipolar pulsed power source can be found elsewhere in the literature [37]. All samples were treated for 30 min under galvanostatic conditions, i.e. the current was kept constant during the entire process and the anode potential was allowed to vary. Sample codes and the corresponding electrical parameters used for each one are presented in Table 1.

Scanning electron microscopy (Hitachi S-3500N operating at 20 kV) was used to study the coating surface morphology and cross sections. The samples were sputter-coated with a gold film before SEM analysis. Coating thickness measurements were performed using an Eddy current gauge. For each sample twenty measurements were taken on the coated surface. Statistical treatments were applied to extract the mean data values and the scatter.

Table 1
Electrical parameters and sample codes for PEO treatment on 6061 Al alloy.

Sample code	Frequency (Hz)	D_t (%)	t_{on} (ms)	*: J (A/dm ²)
S12-*	1000	20	0.2	5, 10, 15, 20, 25
S18-*	1000	80	0.8	
S52-*	50	20	4	
S58-*	50	80	16	

Microhardness measurements were made on polished cross-sections of the PEO coatings using a Vickers diamond indenter mounted on a Buehler Micromet II microhardness tester under loads of 25 and 50 g, applied for 10 s. The average of ten measurements is reported for each microhardness value.

3. Results and discussion

3.1. Voltage–time behavior and coating thickness

Typically, up to four stages are distinguished during the PEO process [28,33,38]. Fig. 1 illustrates the voltage–time response of sample S12–25 containing all four stages.

During *stage I*, an abrupt linear increase in the voltage is observed within a short period of time. This stage is similar to conventional anodization which involves the rapid electrochemical formation of an initial thin oxide film [23,38]. At the end of stage I, the breakdown voltage is reached, which corresponds to the dielectric breakdown of the oxide film.

In *stage II*, after breakdown has occurred, a large number of small micro-discharges with a white color appear, covering the entire surface of the sample evenly. Sparks are characteristic of the PEO process and play a crucial role in the formation of the coatings. Seconds after the beginning of the PEO process, intense gas generation is observed on the surface of the sample. The slope of the voltage–time curve decreases during stage II.

In *stage III*, the rate of voltage change increases as compared to stage II. The micro-discharges become more intense and their color changes from white to yellow and then gradually to orange in subsequent stages of the process.

In *stage IV*, the rate of voltage increase becomes slightly slower than that in stage III. Sparks become even stronger while their population decreases and their color remains orange. It is believed [5,28] that the strong and long-lasting sparks could have a detrimental effect on the coatings in some cases. During stage IV, voltage fluctuations appear in the voltage–time curve, as can be seen in the inset in Fig. 1, and has been reported by other researchers [39,40]. The onset of voltage fluctuations could be considered an indication of the beginning of stage IV.

The voltage–time response of coatings treated at different electrical parameters and the measured thicknesses are illustrated in Figs. 2 and 3. The oxide layers had average thicknesses ranging from 5 to 74 μm . Increasing the current density (J) at constant frequency and duty cycle resulted in thicker coatings.

Comparing the voltage–time response of samples coated at different electrical parameters (Figs. 2 and 3) revealed that increasing the current

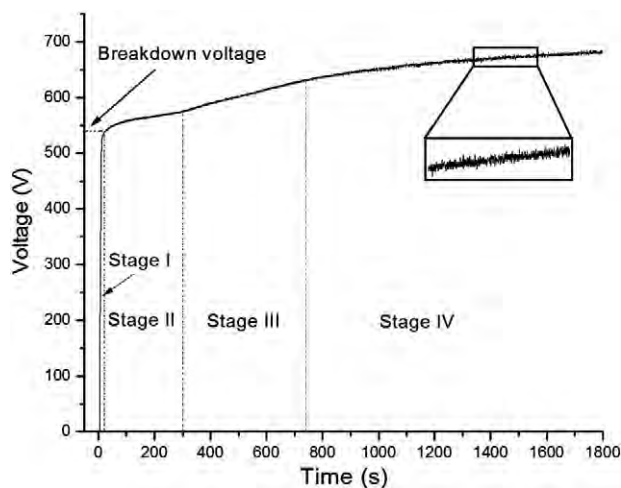


Fig. 1. A typical voltage–time response of a PEO coated 6061 Al alloy sample (S12–25) showing the four different stages occurring during PEO.

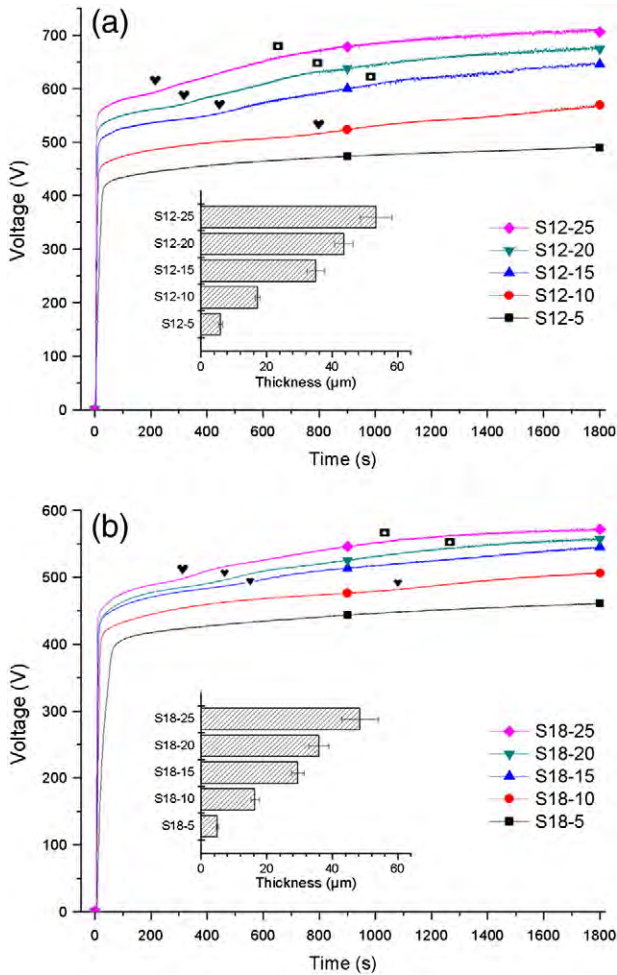


Fig. 2. Voltage–time response and coating thicknesses of (a) samples coated at 1000 Hz and a duty cycle of 20% (S12-*), and (b) samples coated at 1000 Hz and a duty cycle of 80% (S18-*). The approximate onset of stage 3 and 4 are marked with ♥ and ■, respectively.

density from 5 to 25 A/dm² altered the duration and ratio of the different stages during PEO. This variation is more easily distinguished for samples coated at a frequency of 1000 Hz and the approximate onset of stage 3 and 4 has been marked on the voltage–time curves in Fig. 2. As the current density decreased from 25 A/dm², the length of stage II increased and since the total deposition time was constant for all samples, i.e. 30 min, the last two stages became shorter. For sample S12–25, stage II finished after about 200 s from the beginning of the PEO process, while for samples S12–20, S12–15 and S12–10, stage II lasted longer and ended after about 300, 450 and 800 seconds, respectively. The voltage–time response of sample S12–5 had only stages I and II. Almost the same trend can be observed in the voltage–time response of sample sets S18-*, S52-* and S58-* as well. However, for samples S52–15, S52–20, and S52–25, Fig. 3-a, the four stages are not distinguished and it seems that stage 4 has begun soon after the breakdown voltage was reached. Regardless of the frequency and duty cycles applied, samples coated at a current density of 5 A/dm² show only the first two stages in their voltage–time curves.

Fig. 4 compares the maximum and breakdown voltages reached during PEO of each sample. For each column in the figure, the height represents the maximum voltage and the inner column the breakdown voltage for a given sample. Comparing the breakdown and maximum voltages achieved during the PEO of different samples (Fig. 4) revealed that increasing the current density resulted in higher sparking and maximum voltages in each group of samples. Samples coated at a lower duty cycle of 20% had higher sparking and maximum voltages compared to

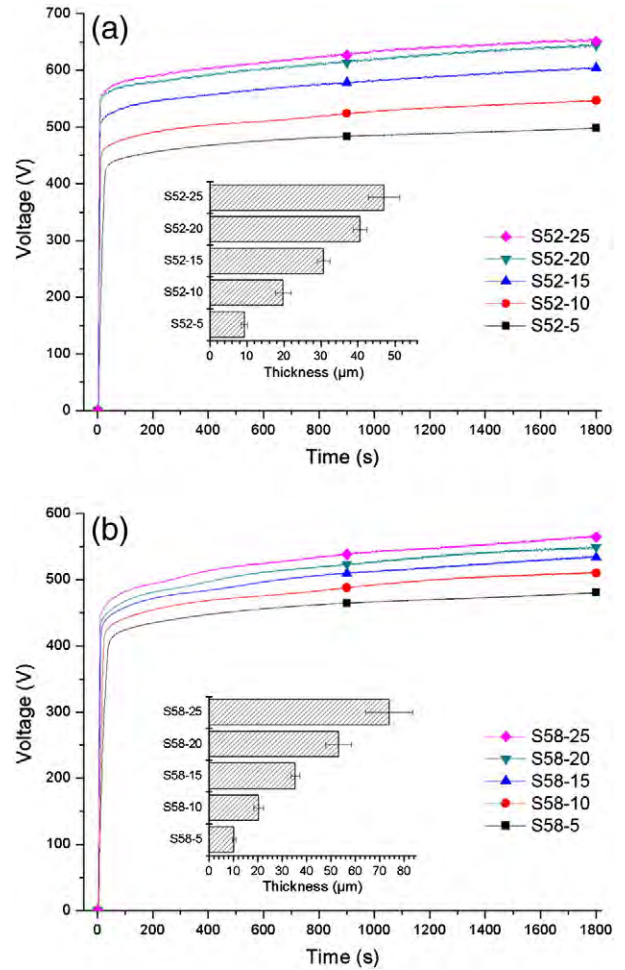


Fig. 3. Voltage–time response and coating thicknesses of (a) samples coated at 50 Hz and a duty cycle of 20% (S52-*), and (b) samples coated at 50 Hz and a duty cycle of 80% (S58-*).

samples coated at a higher duty cycle of 80% at constant frequency and current density.

In a previous study [34] where the effects of applied frequency and duty cycle were investigated at a constant deposition time of 30 min, it was observed that reducing the duty cycle from 80% to 10% decreased the duration of stage II and resulted in longer stage VI and higher breakdown and maximum voltages. Frequency was not found to influence the voltage–time response significantly at constant duty cycle and applied current density.

Altering the applied electrical process parameters changes the duration and ratio of different stages during PEO and as a result would influence the characteristics of the micro-discharges which have different spatial density and intensity during each stage. Micro-discharge characteristics and properties determine the thermal and chemical conditions during PEO and, as a result, play an important role in the morphology, phase formation and composition of the resulting oxide coatings [23].

3.2. Coating surface morphology

The SEM images of the free surfaces and cross sections of the PEO coatings on samples prepared using different electrical conditions are compared in Figs. 5–8. In each section of the figures, the lower part of the picture shows the free surface of the sample, and the upper part shows the corresponding cross section. The surfaces of the coatings in most samples exhibit two distinct regions, a cratered region and clusters of nodular structure, described in detail previously [34]. Craters are the circular areas with a hole in the middle, created by strong micro-

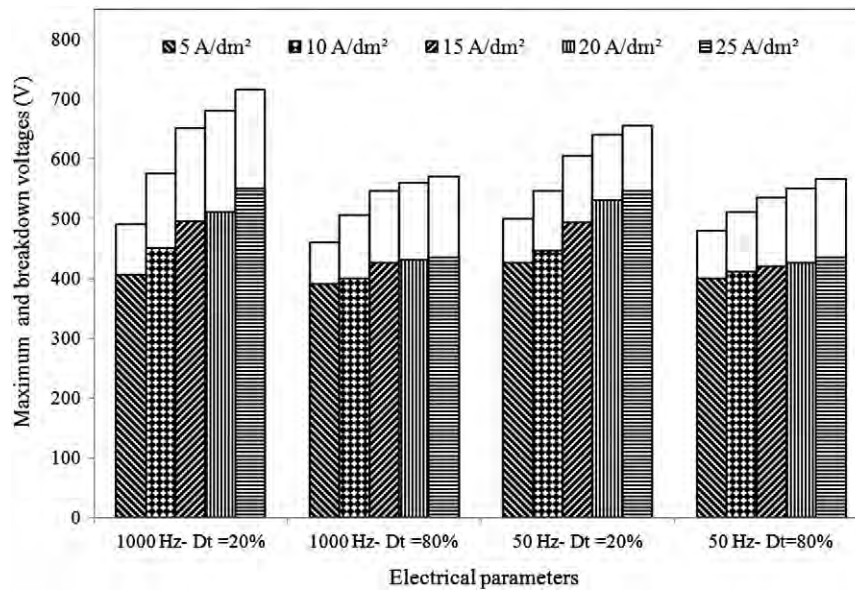


Fig. 4. Maximum and breakdown voltages reached during PEO of 6061 aluminum alloy samples using different electrical parameters (in each column, the height represents the maximum voltage and the inner column represents the breakdown voltage).

discharges, and the nodular structure is composed of patches of lighter gray areas, as marked in Fig. 6-e. The morphology and size of the craters, as well as their ratio relative to the nodular structure, vary depending on the processing conditions applied.

Comparing the surface morphologies of samples coated at different conditions, Figs. 5–8, it can be observed that samples coated at current densities above 5 A/dm² exhibit almost similar morphologies consisting of craters and nodular structures with varying ratios.

Samples coated at a current density of 5 A/dm², S12–5, S18–5, S52–5, and S58–5, contain elongated open pores on the surface of the coatings. This pore morphology was also observed by other researchers on aluminum [41,42] and magnesium [38,43] alloy substrates. Open pores are generally observed at short processing times when the PEO coating

thickness is low. The voltage–time responses of samples treated at 5 A/dm² (Figs. 2 and 3) contain only the first two stages, I and II, and the thickness of these coatings is below 10 μm after 30 min of PEO coating which is considerably lower than for other samples. Formation of the open pores may be due to the low thickness of the coating and good thermal conductivity of the substrate which causes the molten material produced by the micro-discharges to be quickly quenched allowing formation of the open-pore structure [5]. These results indicate that the surface of samples whose voltage–time curve fell in stage II were composed of open micro-pores.

Comparing the surface morphology of samples coated at a frequency of 1000 Hz and a duty cycle of 20%, Fig. 5, b–e, suggests that increasing the current density from 10 to 25 A/dm² affected the morphology of

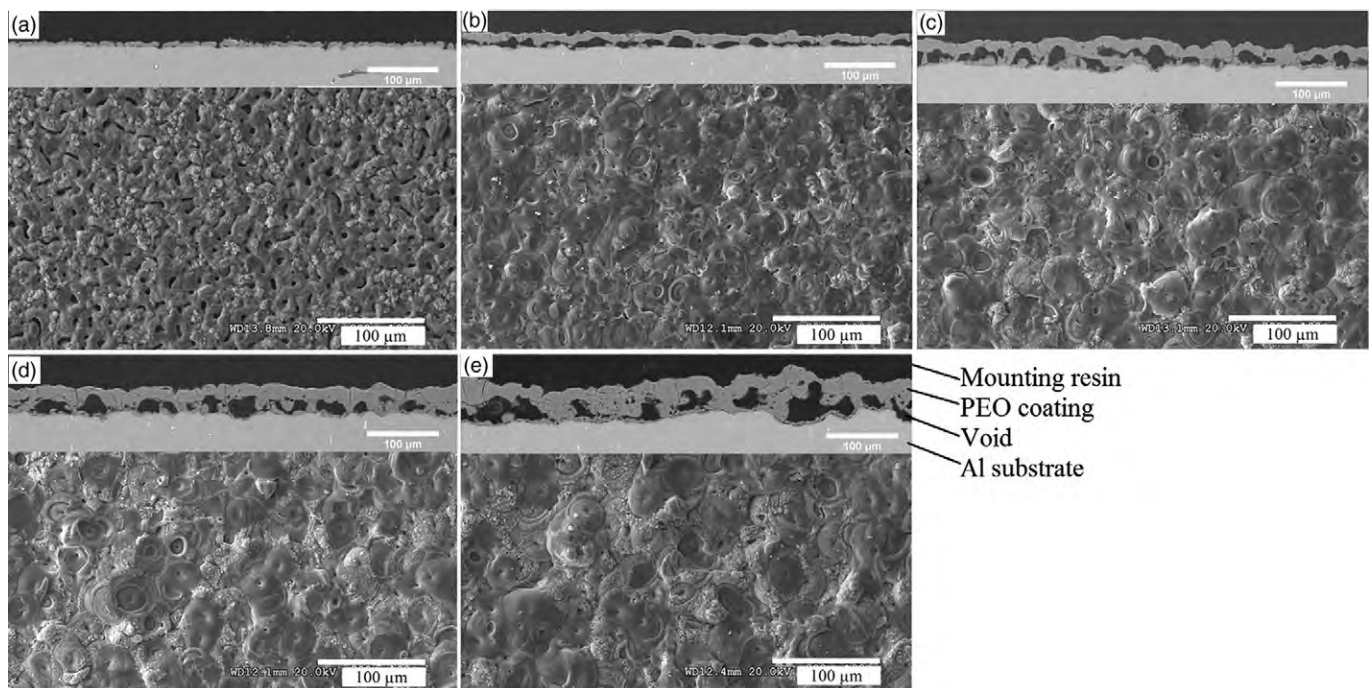


Fig. 5. SEM images of the free surface (lower part) and cross sections (upper part) of coatings prepared at a frequency of 1000 Hz, duty cycle of 20% and different current densities on samples (a) S12–5, (b) S12–10, (c) S12–15, (d) S12–20, and (e) S12–25.

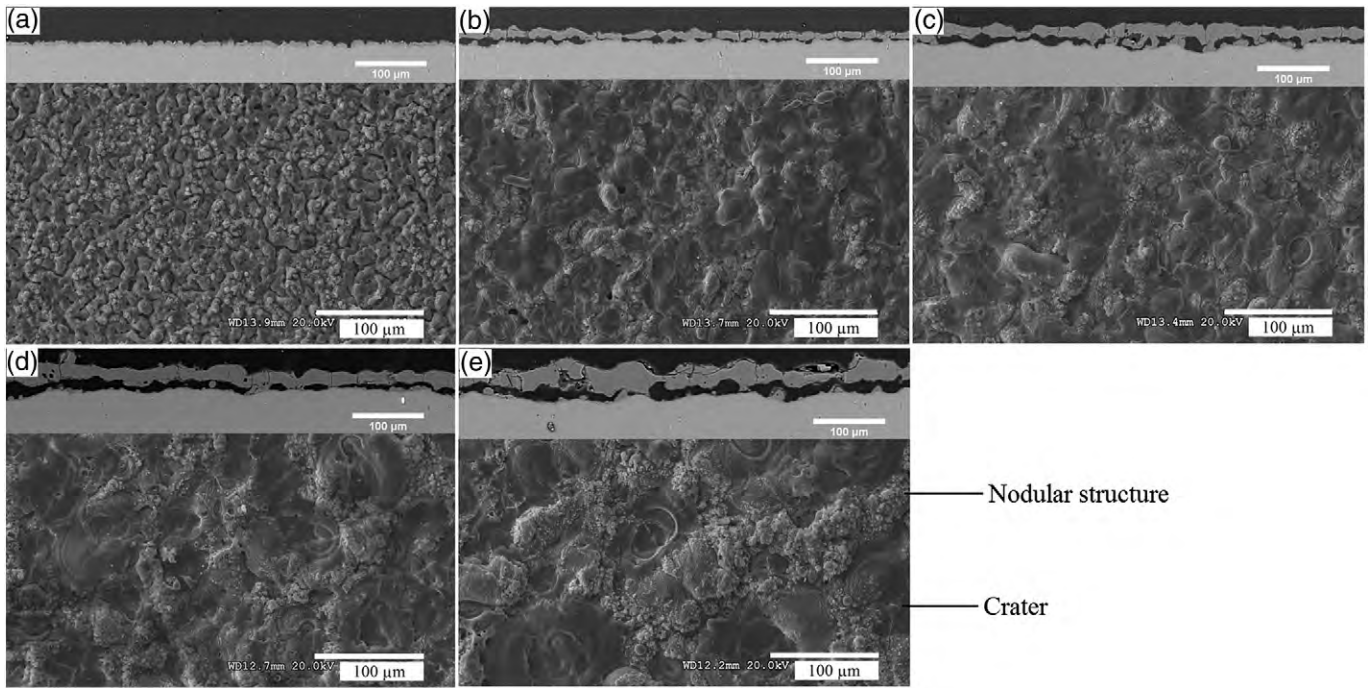


Fig. 6. SEM images of the free surface (upper part) and cross sections (lower part) of coatings prepared at a frequency of 1000 Hz, duty cycle of 80% and different current densities on samples (a) S18–5, (b) S18–10, (c) S18–15, (d) S18–20, and (e) S18–25.

the PEO coatings in addition to their thickness, Fig. 2-a. The surface of sample S12–10 is mainly composed of a large number of craters with very small areas of nodular structure. Each crater has a discharge channel in the centre through which the molten material flowed onto the surface of the coating. The results of EDX analyses on 6061 aluminum alloy substrates coated by PEO in silicate containing electrolytes, suggested that craters were rich in Al, while the nodular structure was rich in Si [34,44].

In samples S12–10 to S12–25, (Fig. 5-b to e) as the current density increased, the size of the craters increased and the nodular structure

covered a larger area fraction of the PEO coating surface. As discussed in Section 3.1, increasing the current density shrank stage II and resulted in a longer stage IV. The surface of the coating on sample S12–10 which was in stage III after 30 min was mainly composed of craters, Fig. 5-b. Samples S12–15, S12–20, and S12–25 were in stage IV after 30 min, Fig. 2-a, and the length of stage IV was extended by increasing the current density. Examining the surface morphology of these samples in Fig. 5, c–d, shows that the relative area fraction of the nodular structure covering the surface of the coating also grew with increasing the current density.

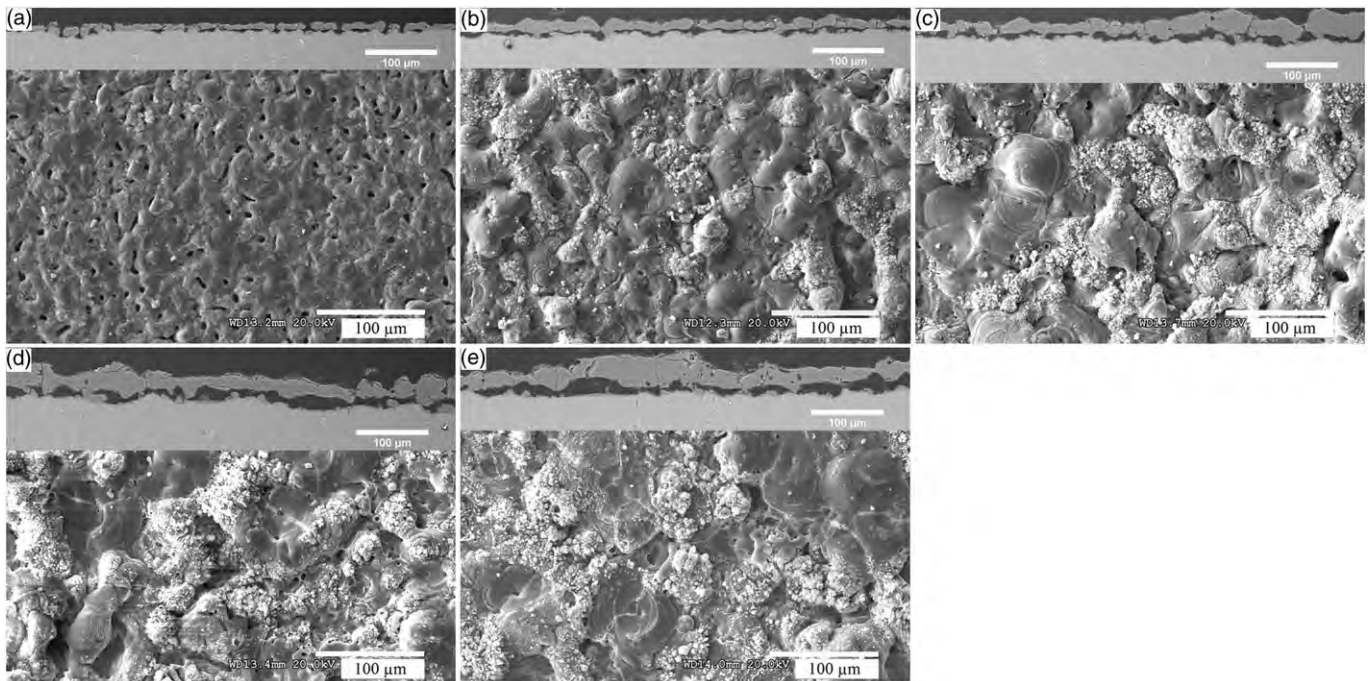


Fig. 7. SEM images of the free surface (upper part) and cross sections (lower part) of coatings prepared at a frequency of 50 Hz, duty cycle of 20% and different current densities on samples (a) S52–5, (b) S52–10, (c) S52–15, (d) S52–20, and (e) S52–25.

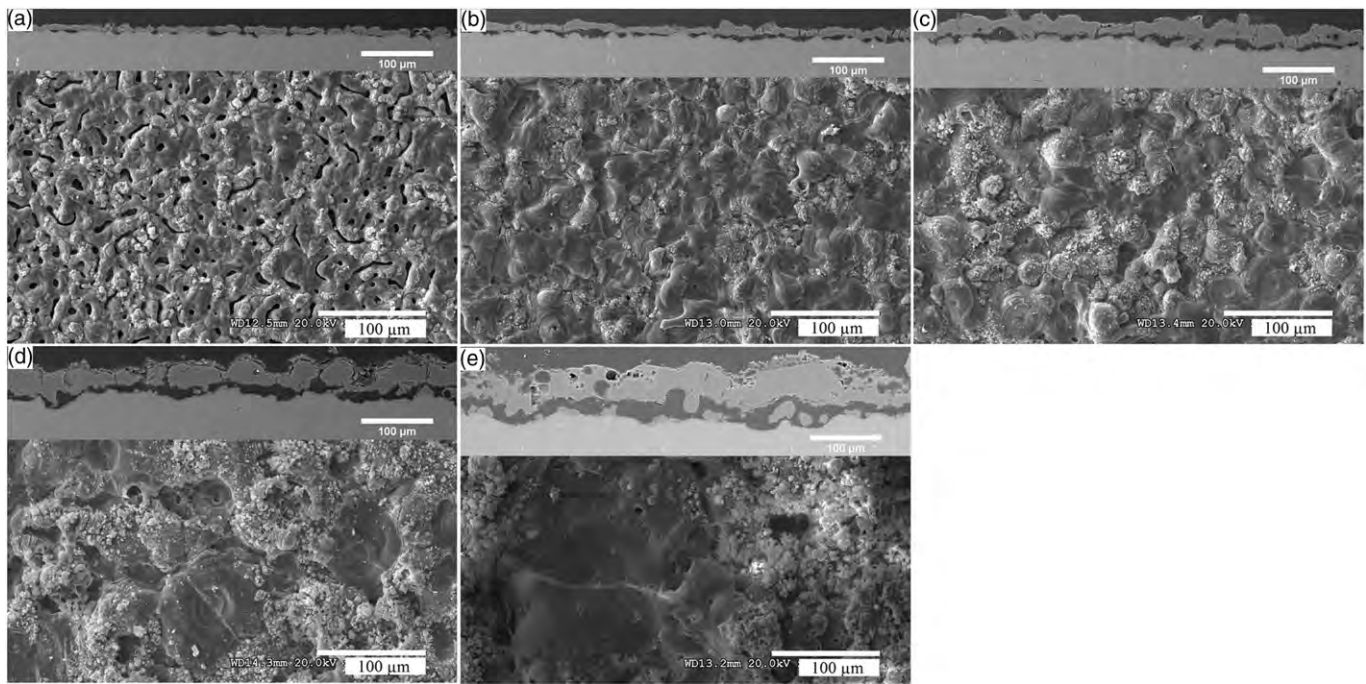


Fig. 8. SEM images of the free surface (lower part) and cross sections (upper part) of coatings prepared at a frequency of 50 Hz, duty cycle of 80% and different current densities on samples (a) S58-5, (b) S58-10, (c) S58-15, (d) S58-20, and (e) S58-25.

Samples S18-* (Fig. 6), coated at the same frequency of 1000 Hz as S12-* but a higher duty cycle of 80%, exhibit the same trend. However, at an equal current density, the craters are bigger in size and the nodular structure covers a larger portion of the coating surface area as compared to samples S12-*.

Samples coated at the lower frequency of 50 Hz and duty cycles of 20% and 80%, Figs. 7 and 8 respectively, follow the same behavior as those coated at 1000 Hz. Again, for both duty cycles of 20% and 80%, higher current densities resulted in thicker coatings, bigger craters, and more nodular structures on the surface of the coatings.

It was observed that at both frequencies, 50 and 1000 Hz, higher duty cycle of 80% (Figs. 6 and 8) produced bigger craters and more nodular structure at a constant current density compared to the lower duty cycle of 20%. These observations are confirmed by a previous study [34] in which EDX elemental maps and measurements of crater radius were used to study the effect of duty cycle on Al/Si ratio and the size of craters on the surface of the samples. The larger crater size in samples coated at higher duty cycle and current densities at both frequencies could be attributed to the effect of the electrical parameters on the coating thickness and structure. Craters are the result of micro-discharges generated by dielectric breakdown at weak and defective spots in the oxide coating and increasing the thickness of the coatings reduces the number of weak sites. The increased size of craters, indicative of stronger micro-discharges, is ascribed to the reduced number of discharging sites through which higher current is able to pass [5,30,45]. The longer t_{on} at the higher duty cycle of 80% compared to lower duty cycle of 20% provides more time for the gases to leave the molten material, thus creating a coating with less porosity and fewer sites for micro-discharges to occur, as evident in cross-sectional SEM images in Figs. 5–8. Increasing J in each set of samples resulted in thicker coatings (Figs. 2 and 3). In a thicker oxide coating, higher energy is required to pass through the coating and with reduced weak points the current is localized in fewer locations, resulting in stronger sparks creating bigger craters [30,34].

3.3. Cross-sectional micro-structures of the coatings

The cross-sections of the PEO coatings examined by SEM are presented in Figs. 5–8 for different processing conditions. PEO coatings are typically comprised of up to three layers. Adjacent to the substrate, there is a very thin inner layer which is termed “the barrier layer” followed by a thicker layer of variable thickness or the “functional layer” which provides the main thermo-mechanical and tribological functionality of the coating [35,46]. In addition to the barrier and functional layer, found in the majority of samples in this study, a third porous and loose layer can also be formed in PEO coatings. The loose outer layer, located on top of the functional layer (Fig. 9-b), was observed on a few samples. The outer loose layer, also reported elsewhere in the literature [46,47], can be removed after PEO treatment to expose the dense functional layer [48]. However, it is suggested that the porosity in the outer loose layer could be used as a base for sealants and primers for corrosion protection [35].

For all samples, the interface between the coatings and the substrate had a wavy appearance which might be the result of dissolution of the substrate in the early stages of the process [49] given the high pH (around 12) of the electrolyte. Large pores, which are connected in some areas and possibly enlarged during polishing, are present between the inner and outer layers of the coatings (the dark area between the barrier layer and functional layer in Fig. 9-b). Coatings with similar cross-sectional structure containing large pores between the inner and outer layers were also observed in studies using PEO on aluminum [29,50] and magnesium [51,52] alloy substrates, specifically when applying a DC or unipolar pulsed DC current modes. On the other hand, such a pore structure was not observed in coatings on titanium alloys after PEO [32]. Such morphology is normally not observed when using the bipolar pulsed DC mode. In studies investigating the effect of current mode on the microstructure of PEO coatings [52–55], the improved quality of coatings produced using a bipolar pulsed DC compared to a unipolar pulsed DC was attributed to the fact that, in the bipolar pulsed

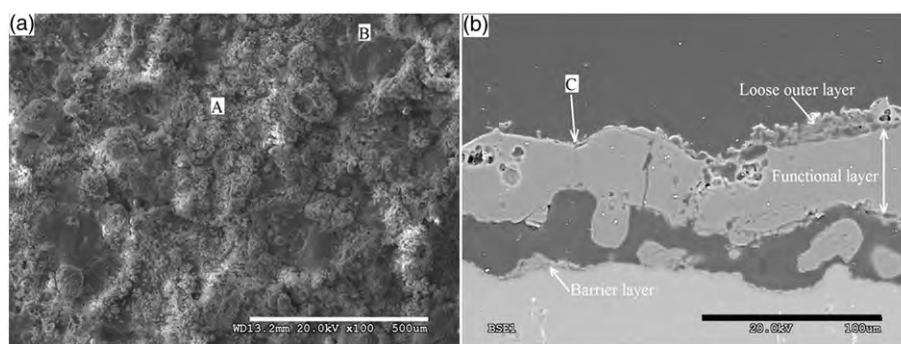


Fig. 9. SEM images showing (a) the free surface, and (b) the cross-section of sample S58–25.

DC mode, the strongest plasma discharges and the average plasma temperature were reduced resulting in a more compact structure with fewer defects.

A possible mechanism for the formation of pores between the inner and outer layers of the coatings when a unipolar pulsed DC is employed can be proposed. Aluminum is a reactive metal with a negative standard electrode potential of -1.66 vs. SHE, but the oxide film formed on aluminum is protective in the pH range ~ 4 to 8.5 as indicated by the Pourbaix diagram. However, acids and bases can attack the protective film leading to the dissolution of the base metal [56]. It was previously reported that increasing the concentration of KOH in the electrolyte decreased the film growth rate on an aluminum substrate significantly due to the increased rate of anodic dissolution [57]. In the early stages of the PEO process, after the breakdown voltage has been reached, micro-discharges are formed on the surface of the substrate. Each micro-discharge ejects molten materials out on to the surface and since the coating is still thin and in contact with the aluminum substrate with a high thermal conductivity, the molten material solidifies very rapidly, creating open micropores on the surface. Examination of the surface morphologies of samples coated at a current density of 5 A/dm^2 (S12–5, S18–5, S52–5, and S58–5), Fig. 5 to Fig. 8, reveals that all these samples contain open micropores and the coating thicknesses are less than $10 \mu\text{m}$ (Figs. 2 and 3). As the coating thickens, less heat is transferred to the aluminum substrate since more is absorbed by the coating, allowing the molten material to solidify more slowly thus creating the typical crater structure. The alkaline electrolyte used has a high pH of ~ 12 , which is well above the pH range in which the aluminum oxide film formed is protective. The alkaline electrolyte can reach the underlying layers through the open pores formed in the early stages of the process leading to dissolution of the coating and corrosion of the substrate and the creation of the voids observed. The negative portion of the pulse in the pulsed bipolar current mode can inhibit the transformation of the coating to easily dissolved compounds or prevent direct dissolution of the coating [58].

It is worth noting that although the pulsed bipolar current mode produces denser coatings with enhanced tribomechanical properties, the coating porosity could be an asset in applications such as polymer-ceramic composite coatings and thermal barrier coatings.

SEM images of the cross-sections of PEO coatings (Figs. 5–8) show channels across the coatings created by individual discharge events and also scattered pores in the functional layer. Pores may form due to the entrapment of oxygen [59] or other types of gases that are formed during the strong discharges [29] in molten alumina.

The coatings produced with the shortest t_{on} time, Fig. 5, contain more porosity and discharge channels in the coatings as compared to other samples coated at longer t_{on} times. This is more obvious when comparing the cross-sectional microstructure of S12–25 (Fig. 5-e) produced at a t_{on} time of 0.2 ms with S18–25 (Fig. 6-e), S52–25 (Fig. 7-e),

and S58–25 (Fig. 8-e) with t_{on} times of 0.8 , 4 , and 16 ms , respectively. The longer t_{on} times can create longer strong discharges which would make it easier for the gases to escape the molten material and could result in a better sintering and thus denser coating.

The coating growth is the result of the molten materials flowing through discharge channels. The central hole in the cratered regions is the discharge channel through which the molten material was ejected and rapidly solidified upon contact with the electrolyte [54,60]. Area “C” in Fig. 9-b shows a discharge channel in the coating cross section that created a crater (Area “B” in Fig. 9-a) in sample S58–25. The coating growth rate is a function of the number and intensity of discharge channels. Thickness measurements (Figs. 2 and 3) show that the coating growth rate increased when higher current densities were applied in each set of samples. The average thickness of sample S58–25 (Fig. 3-b), $\sim 74 \mu\text{m}$, was considerably higher than other samples. The SEM image of the free surface of S58–25 show that the nodular structure (as seen in Area “A” in Fig. 9-a) covered a large portion of the area in this sample. The cross-sectional view of S58–25 in Fig. 9-b revealed that the loose outer layer is actually the nodular structure with a thickness high enough to be observed in the cross section of the coating. The presence of the thicker nodular structure forming the loose outer layer in S58–25 could be one of the reasons for the high thickness readings on this sample. A previous study of phase composition and distribution in PEO coatings prepared with conditions similar to the present work [37], showed the outer surface was composed of mullite and amorphous phases. The loose outer layer is an incomplete layer of nodular structure clusters on the surface and is therefore not suitable for applications where good mechanical properties are required: e.g., wear applications. Due to its poor bonding to the functional layer as a result of interfacial porosity, the outer loose layer can be easily removed when in contact with a sliding surface and should be removed prior to application to expose the inner functional layer with superior wear resistance [46,50].

The outer loose layer was also observed in some areas in the cross sectional views of other samples coated at high current densities, namely samples S18–25, S52–20, S52–25, and S58–20 in Figs. 6-e, 7-d-e, and 8-d, respectively, but its thickness was lower than that of sample S58–25.

In a detailed study on the effect of electrical parameters on phase formation and distribution in PEO coatings on 6061 aluminum substrate [37] it was found that increasing the pulse on-time by employing a lower frequency and higher duty cycle resulted in coatings containing mullite and an amorphous phase in addition to α - and γ - Al_2O_3 . Depth profiling of the coated samples suggested that mullite ($3\text{Al}_2\text{O}_3\text{-}2\text{SiO}_2$) and the amorphous phase were concentrated near the outer surface of the coatings. The formation of mullite and Si-rich amorphous phase was attributed to increased Si concentration as a result of longer pulse on-time. Our proposed mechanism [34] suggests that when t_{on} is long, the negative ions like SiO_3^{2-} have more time to get adsorbed on the

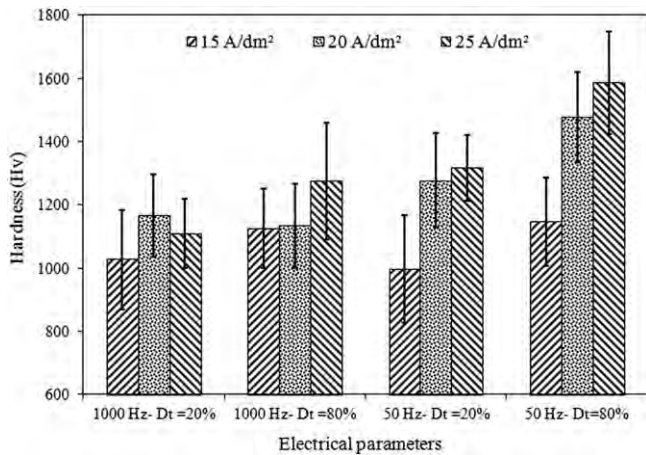


Fig. 10. Cross sectional Vickers microhardness values in functional layer of PEO coatings on 6061 Al alloy as a function of electrical parameters.

surface of the anode. This, in addition to lower spatial density of sparks on the surface of samples coated at longer t_{on} times, would result in higher concentration of Si rich species on the surface of the coatings.

3.4. Coating microhardness

Microhardness values determined from Vickers indentations on the cross sections of the coatings in the functional layer areas are given in Fig. 10. Coatings on samples treated at current densities of 5 and 10 A/dm² were very thin compared to the size of the indentation. To prevent error in the readings caused by low thickness, only hardness values of samples with enough thickness are reported.

The average coating hardness values ranged from 1000 Hv (9.8 GPa) to around 1600 Hv (15.7 GPa) in sample S58–25. These values are appreciably higher than the hardness of conventional anodising coatings (~4–6 GPa [61,62]). The improved hardness of PEO coatings compared to conventional anodic alumina is attributed to the reduced porosity and the existence of crystalline alumina phases, namely α -Al₂O₃. PEO coatings on aluminum alloys are normally a mixture of α -Al₂O₃ (~26 GPa), γ -Al₂O₃ (~17 GPa), mullite (~10.5 GPa), and amorphous alumina (~4–6 GPa) [50,60,63]. The measured hardness in PEO coatings is lower than in dense bulk alumina phases due to the presence of porosity caused by the entrapment of gases in the coating during the treatment process, and channels created by individual micro-discharges (demonstrated in Fig. 9-b) in PEO coatings.

The microhardness test results (Fig. 10) suggest that increasing t_{on} resulted in higher average hardness values. As given in Table 1, t_{on} duration for S12–*, S18–*, S52–*, and S58–* samples are 0.2, 0.8, 4, and 16 ms, respectively. It can also be deduced from Fig. 10 that except for S12–* samples, coated at a frequency of 1000 Hz and a D_t of 20%, in all other samples increasing the current density from 15 to 25 A/dm² resulted in higher average hardness.

The hardness of the PEO coating is a function of the nature of the dominant phases present, as well as their ratio and distribution, and the porosity and density of micro-cracks in the coatings. As discussed in Section 3.3, the coatings produced at 1000 Hz and a duty cycle of 20% had the shortest t_{on} time (0.2 ms) and contained more porosity and discharge channels in the coatings (Fig. 5) as compared to other samples coated at longer t_{on} times. Longer t_{on} times can create longer discharges, making it easier for the gases to escape the molten material thus causing better sintering and a denser coating. It was previously reported [37] that increasing the pulse on-time and current density enhanced the $\gamma \rightarrow \alpha$ -Al₂O₃ phase transformation resulting in more α -Al₂O₃, which is the hardest alumina phase, in the coatings. Coatings on samples PEO treated at a frequency of 1000 Hz and a duty cycle of 20% with different current densities contained essentially

only γ -Al₂O₃. Increasing the duty cycle to 80% at the same frequency resulted in the formation of α -Al₂O₃ in addition to γ -Al₂O₃. In samples treated at 50 Hz, α -Al₂O₃ was identified in all samples at a current density greater than 5 A/dm² in addition to γ -Al₂O₃.

PEO coatings on samples treated at 1000 Hz contained a higher level of porosity and micro-cracks with respect to other samples (Fig. 5). Variation in the coating microhardness values of S12–* samples is possibly more dependent on the amount of porosity and micro-cracks in these coatings since the phase composition of these coating was the same and composed only of γ -Al₂O₃. In other samples, however, the microhardness seems to be influenced by phase composition and content more than porosity because the cross sectional SEM micrographs (Figs. 6–8) show relatively dense structures in the functional layer of the coatings. In samples S18–*, S52–*, and S58–*, the relative α -Al₂O₃ content in the coating increased by applying a longer t_{on} and higher current density [37] which is indicative of the positive effect of increased relative content of α -Al₂O₃ on the coating hardness.

4. Conclusions

PEO was performed on the 6061 aluminum alloy in an alkaline silicate electrolyte using a pulsed unipolar current mode under galvanostatic conditions. Samples were coated at different frequencies, duty cycles, and current densities. For each sample the voltage–time response of the PEO process was obtained and compared with the surface morphology, cross-sectional view, and thickness of the coating. Vickers microhardness test was used to study the effect of the electrical parameters on the hardness of the coatings. Special consideration was given to the connection between the electrical parameters, different stages of the PEO process, and the morphology and microstructure of the coatings. The following conclusions can be drawn from this study:

1. Voltage–time curves of samples coated with different electrical parameters showed up to four different stages. Applying different electrical parameters changed the duration and ratio of these stages during PEO and affected the surface morphologies of the coatings.
2. The surfaces of the coatings in most samples exhibited two distinct regions, craters and clusters of nodular structure. The size of the craters, as well as the area fraction of the cratered region and the nodular structure changed when different electrical parameters were applied.
3. For samples treated at a current density of 5 A/dm² the voltage–time curves exhibited only two stages, I and II. Elongated open micropores were observed on the surface of all these samples. The low thickness of the coating together with the good thermal conductivity of the substrate could suggest the formation of such pores is due to the rapid solidification of the molten material.
4. Increasing the current density from 10 to 25 A/dm² decreased the duration of stage II and increased the extent of the last stage in the voltage–time response resulting in bigger craters and increased area fractions of the nodular structure on the PEO coating surfaces.
5. The application of higher current densities and longer pulse-on times, by employing higher duty cycles and a lower frequency, improved the microhardness of the coatings. This could be due to an enhanced $\gamma \rightarrow \alpha$ -Al₂O₃ phase transformation resulting in more α -Al₂O₃ in the oxide layer and an increased density of the functional layer due to the reduction of porosity.

Acknowledgments

This research was supported by the National Research Council Canada (NRC) and Ontario Graduate Scholarship (OGS). The authors would like to thank Marco Zeman and Mike Meinert (of Automotive and Surface Transportation, National Research Council Canada, London, ON, Canada) for their help with the tests.

References

- [1] D. Shen, G. Li, C. Guo, J. Zou, J. Cai, D. He, et al., *Appl. Surf. Sci.* 287 (2013) 451–456.
- [2] F. Monfort, A. Berkani, E. Matykina, P. Skeldon, G.E. Thompson, H. Habazaki, et al., *Corros. Sci.* 49 (2007) 672–693.
- [3] J.A. Curran, H. Kalkanci, Y. Magurova, T.W. Clyne, *Surf. Coat. Technol.* 201 (2007) 8683–8687.
- [4] Y. Cheng, E. Matykina, R. Arrabal, P. Skeldon, G.E. Thompson, *Surf. Coat. Technol.* 206 (2012) 3230–3239.
- [5] Y. Cheng, F. Wu, E. Matykina, P. Skeldon, G.E.E. Thompson, *Corros. Sci.* 59 (2012) 307–315.
- [6] W. Simka, M. Sowa, R.P. Socha, A. Maciej, J. Michalska, *Electrochim. Acta* 104 (2012) 518–525.
- [7] M. Petković, S. Stojadinović, R. Vasilčić, L. Zeković, *Appl. Surf. Sci.* 257 (2011) 10590–10594.
- [8] C. Wang, F. Wang, Y. Han, *Surf. Coat. Technol.* 214 (2013) 110–116.
- [9] Y. Cheng, F. Wu, J. Dong, X. Wu, Z. Xue, E. Matykina, et al., *Electrochim. Acta* 85 (2012) 25–32.
- [10] L.R. Krishna, A.S. Purnima, G. Sundararajan, *Wear* 261 (2006) 1095–1101.
- [11] M. Treviño, R.D. Mercado-Solis, R. Colás, A. Pérez, J. Talamantes, A. Velasco, *Wear* 301 (2012) 434–441.
- [12] G. Rapheal, S. Kumar, C. Blawert, N.B. Dahotre, *Wear* 271 (2011) 1987–1997.
- [13] X. Li, X. Liu, B.L. Luan, *Appl. Surf. Sci.* 257 (2011) 9135–9141.
- [14] S. Moon, *J. Solid State Electrochem.* (2013) 3–8.
- [15] W. Xue, C. Wang, H. Tian, Y. Lai, *Surf. Coat. Technol.* 201 (2007) 8695–8701.
- [16] T. Akatsu, T. Kato, Y. Shinoda, F. Wakai, *Surf. Coat. Technol.* 223 (2013) 47–51.
- [17] J.A. Curran, T.W. Clyne, *Surf. Coat. Technol.* 199 (2005) 177–183.
- [18] F.-Y. Jin, K. Wang, M. Zhu, L.-R. Shen, J. Li, H.-H. Hong, et al., *Mater. Chem. Phys.* 114 (2009) 398–401.
- [19] Y. Yan, J. Sun, Y. Han, D. Li, K. Cui, *Surf. Coat. Technol.* 205 (2010) 1702–1713.
- [20] A. Krzakała, K. Służalska, M. Widziołek, J. Szade, A. Winiarski, G. Dercz, et al., *Electrochim. Acta* 104 (2013) 407–424.
- [21] S.A. Alves, R. Bayón, A. Igartua, V.S. De Viteri, L.A. Rocha, Tribocorrosion behaviour of anodic titanium oxide films produced by plasma electrolytic oxidation for dental implants, *Lubr. Sci.* 26 (2014) 500–513.
- [22] A.L. Yerokhin, L.O. Snizhko, N.L. Gurevina, A. Leyland, A. Pilkington, A. Matthews, *Surf. Coat. Technol.* 177–178 (2004) 779–783.
- [23] J. Jovović, S. Stojadinović, N.M. Šišović, N. Konjević, *J. Quant. Spectrosc. Radiat. Transf.* 113 (2012) 1928–1937.
- [24] S. Stojadinović, R. Vasilčić, M. Petković, I. Belča, B. Kasalica, M. Perić, et al., *Electrochim. Acta* 59 (2012) 354–359.
- [25] E. Matykina, A. Berkani, P. Skeldon, G.E. Thompson, *Electrochim. Acta* 53 (2007) 1987–1994.
- [26] M. Göttlicher, M. Rohnke, A. Helth, T. Leichtweiß, T. Gemming, A. Gebert, et al., *Acta Biomater.* 9 (2013) 9201–9210.
- [27] S. Stojadinović, R. Vasilčić, M. Petković, I. Belča, B. Kasalica, M. Perić, et al., *Electrochim. Acta* 79 (2012) 133–140.
- [28] R.O. Hussein, X. Nie, D.O. Northwood, A. Yerokhin, A. Matthews, *J. Phys. D. Appl. Phys.* 43 (2010) 105203–105216.
- [29] R.O. Hussein, D.O. Northwood, X. Nie, *J. Vac. Sci. Technol. A* 28 (2010) 766–773.
- [30] S. Stojadinovic, R. Vasilic, I. Belca, M. Petkovic, B. Kasalica, Z. Nedic, et al., *Corros. Sci.* 52 (2010) 3258–3265.
- [31] L. Wang, L. Chen, Z. Yan, W. Fu, *Surf. Coat. Technol.* 205 (2010) 1651–1658.
- [32] R.O. Hussein, X. Nie, D.O. Northwood, *Mater. Chem. Phys.* 134 (2012) 484–492.
- [33] L. Wang, X. Nie, *Thin Solid Films* 494 (2006) 211–218.
- [34] V. Dehnavi, B.L. Luan, D.W. Shoesmith, X.Y. Liu, S. Rohani, *Surf. Coat. Technol.* 226 (2013) 100–107.
- [35] E. Matykina, R. Arrabal, A. Mohamed, P. Skeldon, G.E. Thompson, *Corros. Sci.* 51 (2009) 2897–2905.
- [36] Y.K. Pan, C.Z. Chen, D.G. Wang, X. Yu, *J. Biomed. Mater. Res. B Appl. Biomater.* 100 (2012) 1574–1586.
- [37] V. Dehnavi, X.Y. Liu, B.L. Luan, D.W. Shoesmith, S. Rohani, *Surf. Coat. Technol.* 251 (2014) 106–114.
- [38] R.O. Hussein, X. Nie, D.O. Northwood, *Electrochim. Acta* 112 (2013) 111–119.
- [39] F. Monfort, E. Matykina, A. Berkani, P. Skeldon, G.E. Thompson, H. Habazaki, et al., *Surf. Coat. Technol.* 201 (2007) 8671–8676.
- [40] Y. Guan, Y. Xia, G. Li, *Surf. Coat. Technol.* 202 (2008) 4602–4612.
- [41] G. Sundararajan, L. Rama Krishna, *Surf. Coat. Technol.* 167 (2003) 269–277.
- [42] S. Moon, Y. Jeong, *Corros. Sci.* 51 (2009) 1506–1512.
- [43] U. Malayoglu, K.C. Tekin, S. Shrestha, *Surf. Coat. Technol.* 205 (2010) 1793–1798.
- [44] M.M.S. Al Bosta, K. Ma, H. Chien, *Infrared Phys. Technol.* 60 (2013) 323–334.
- [45] W. Xue, Z. Deng, Y. Lai, R. Chen, *J. Am. Ceram. Soc.* 81 (1998) 1365–1368.
- [46] F.C. Walsh, C.T.J. Low, R.J.K. Wood, K.T. Stevens, J. Archer, A.R. Poeton, et al., *Trans. Inst. Met. Finish.* 87 (2009) 122–135.
- [47] A.L. Yerokhin, A. Shatrov, V. Samsonov, P. Shashkov, A. Pilkington, A. Leyland, et al., *Surf. Coat. Technol.* 199 (2005) 150–157.
- [48] E. Matykina, R. Arrabal, P. Skeldon, G.E. Thompson, *Electrochim. Acta* 54 (2009) 6767–6778.
- [49] R.O. Hussein, X. Nie, D.O. Northwood, *Mater. Chem. Phys.* 134 (2012) 484–492.
- [50] Y. Cheng, Z. Xue, Q. Wang, X.-Q. Wu, E. Matykina, P. Skeldon, et al., *Electrochim. Acta* 107 (2013) 358–378.
- [51] Y. Gao, A. Yerokhin, A. Matthews, *Surf. Coat. Technol.* 234 (2013) 132–142.
- [52] R.O. Hussein, D.O. Northwood, J.F. Su, X. Nie, *Surf. Coat. Technol.* 215 (2013) 421–430.
- [53] R.O. Hussein, X. Nie, D.O. Northwood, *Surf. Coat. Technol.* 205 (2010) 1659–1667.
- [54] F. Jaspard-mécuson, T. Czerwiec, G. Henrion, T. Belmonte, L. Dujardin, A. Viola, et al., *Surf. Coat. Technol.* 201 (2007) 8677–8682.
- [55] L. Wang, J. Zhou, J. Liang, J. Chen, *Appl. Surf. Sci.* 280 (2013) 151–155.
- [56] Y. Cheng, M. Mao, J. Cao, Z. Peng, *Electrochim. Acta* 138 (2014) 417–429.
- [57] L. Snizhko, A. Yerokhin, A. Pilkington, N. Gurevina, D. Misnyankin, A. Leyland, et al., *Electrochim. Acta* 49 (2004) 2085–2095.
- [58] J. Chen, Z. Wang, S. Lu, *Rare Met.* 31 (2012) 172–177.
- [59] J.A. Curran, T.W. Clyne, *Acta Mater.* 54 (2006) 1985–1993.
- [60] R.H.U. Khan, A. Yerokhin, X. Li, H. Dong, A. Matthews, *Surf. Coat. Technol.* 205 (2010) 1679–1688.
- [61] G. Alcalá, P. Skeldon, G.E. Thopson, A.B. Mann, H. Habazaki, K. Shimizu, *Nanotechnology* 13 (2002) 451–455.
- [62] P.U. Skeldon, H.W. Wang, G.E. Thompson, *Wear* 206 (1997) 187–196.
- [63] H. Kalkanci, S.C. Kurnaz, *Surf. Coat. Technol.* 203 (2008) 15–22.